Journal of the Mechanical Behavior of Biomedical Materials 77 (2018) 360–374

Contents lists available at ScienceDirect

Journal of the Mechanical Behavior of Biomedical Materials

journal homepage: www.elsevier.com/locate/jmbbm

Bio-corrosion behavior and mechanical characteristics of magnesium-titania-hydroxyapatite nanocomposites coated by magnesium-oxide flakes and silicon for use as resorbable bone fixation material

Shahrouz Zamani Khalajabadi[a,b,*], Aminudin Bin Haji Abu[a,**], Norhayati Ahmad[b], Muhammad Azizi Mat Yajid[b], Norizah Bt Hj Redzuan[b], Rozita Nasiri[c], Waseem Haider[d], Iman Noshadi[e]

[a] Malaysia-Japan International Institute of Technology (MJIIT), Universiti Teknologi Malaysia (UTM), Kuala Lumpur, Malaysia
[b] Department of Materials, Manufacturing and Industrial Engineering, Faculty of Mechanical Engineering, Universiti Teknologi Malaysia (UTM), 81310 Johor Bahru, Johor, Malaysia
[c] Faculty of Chemical Engineering, Universiti Teknologi Malaysia (UTM), 81310 Johor Bahru, Johor, Malaysia
[d] School of Engineering and Technology, Central Michigan University, Mount Pleasant, MI 48859, United States
[e] Department of Chemical Engineering, Rowan University, Glassboro, NJ, United States

ARTICLE INFO

Keywords:
Mg/TiO_2-based nanocomposite
Si/MgO coating
Adhesion strength
UCS
Immersion
Cell viability

ABSTRACT

This study was aimed to improve of the corrosion resistance and mechanical properties of $Mg/15TiO_2/5HA$ nanocomposite by silicon and magnesium oxide coatings prepared using a powder metallurgy method. The phase evolution, chemical composition, microstructure and mechanical properties of uncoated and coated samples were characterized. Electrochemical and immersion tests used to investigate the in vitro corrosion behavior of the fabricated samples. The adhesion strength of ~36 MPa for MgO and ~32 MPa for Si/MgO coatings to substrate was measured by adhesion test. Fabrication a homogenous double layer coating with uniform thicknesses consisting micro-sized particles of Si as outer layer and flake-like particles of MgO as the inner layer on the surface of $Mg/15TiO_2/5HA$ nanocomposite caused the corrosion resistance and ductility increased whereas the ultimate compressive stress decreased. However, after immersion in SBF solution, Si/MgO-coated sample indicates the best mechanical properties compared to those of the uncoated and MgO-coated samples. The increase of cell viability percentage of the normal human osteoblast (NHOst) cells indicates the improvement in biocompatibility of $Mg/15TiO_2/5HA$ nanocomposite by Si/MgO coating.

1. Introduction

Design of novel materials for orthopedic applications with in situ degradability characteristic in physiological environment is aim of extensive researches in the last years (Meischel et al., 2016; Mostaed et al., 2016). Due to the ability of magnesium to solve the biodegradability, stress shielding and osteocompatibility problems, as well as the similar mechanical properties to human bone, it attracted a lot of interest as a replacement orthopedic implant materials to clinical applications over other traditional metallic materials (Dezfuli et al., 2017; Del Campo et al., 2017; Rosalbino et al., 2010; Song, 2007; Wolf and Cittadini, 2003; Nayak et al., 2016; Zhang et al., 2010; Zheng et al., 2014). However, because of the high degradation rate of magnesium in living body environment, the magnesium-based implant lost its mechanical strength before healing of the injured tissue, which could not afford effective biomechanical support and match the bone reconstruction (Ibrahim et al., 2017; Zhang et al., 2016a). In addition to the high corrosion rate, the low bioactivity of magnesium implants as the ability to form hydroxyapatite (HA) is another challenging problem, which need to be resolved before utilization in clinical applications (Chen et al., 2015). To overcome this drawback, several surface modification techniques, i.e. electrochemical deposition (Liu et al., 2012; Mohedano et al., 2015), polymer treatment (Qi et al., 2016; Zomorodian et al., 2013), chemical deposition (Lin et al., 2016; Lu et al., 2012), and micro-arc oxidation (MAO) techniques (Gu et al., 2011; Krishna et al., 2015; Lin et al., 2013), have been introduced to improve the degradation rate and bioactivity of magnesium and its alloys. As is known, fabrication of magnesium-based composites with

* Corresponding author at: Malaysia-Japan International Institute of Technology (MJIIT), Universiti Teknologi Malaysia (UTM), Kuala Lumpur, Malaysia.
** Corresponding author.
E-mail addresses: shahroozzamany@yahoo.com, zkshahrouz2@liveutm.onmicrosoft.com (S.Z. Khalajabadi), aminudin.kl@utm.my (A.B.H. Abu).

http://dx.doi.org/10.1016/j.jmbbm.2017.09.032
Received 22 August 2017; Received in revised form 21 September 2017; Accepted 25 September 2017
Available online 27 September 2017
1751-6161/

bio-ceramic additives (Khalajabadi et al., 2017), besides the surface modification of magnesium implants, and alloying magnesium with biocompatible metals (Fintova et al., 2015; Shi et al., 2015a, 2015b) are the major techniques to protect the implant from fast corrosion and degradation in vivo. Moreover, bio-additives and suitable coatings can improve the hemocompatibility and bioactivity of implants in this field (Heublein et al., 2003; Li et al., 2010; Paital and Dahotre, 2009; Zartner et al., 2007). Gu et al. reported that pure Mg as the matrix materials, and HA as the bio-ceramic additive, were selected to fabricate the Mg/HA biocomposite with different amount of HA content using the powder metallurgy (PM) route. The cytotoxicity tests indicated that Mg/10HA extract showed no toxicity to L-929 cells (Gu et al., 2010).

In our previous work, magnesium-matrix composites with titania and hydroxyapatite reinforcements were developed, as well as an enhancement in degradation resistance and mechanical properties was achieved by addition titania. According to the cell culture results, the Mg/15TiO_2/5HA nanocomposite was biocompatible with osteoblasts (Khalajabadi et al., 2016). As was reported by Li et al., the silicon coating was deposited on the surface of WE43 Mg alloy using PECVD technique to slow down its degradation rate for medical application (Li et al., 2013). Moreover, the corrosion resistance and mechanical properties of Mg/HA/TiO_2/MgO nanocomposites were enhanced by Si mono-layer and Si/ZnO double layer coatings that were fabricated using Radio Frequency Magnetron Sputtering technique (Khalajabadi et al., 2015). Silicon (Si), as an essential mineral in human bodies, is substituted alone or in combination with a variety of other materials for filling bone defects (Khan et al., 2014). In the early stage of bone calcification, silicon was involved according to the reports of Carlisle (Carlisle 1970) and Schwarz and Milne (Schwarz and Milne 1972). Moreover, the stimulation of cell proliferation by Mg and Si ionic products was found by Wu and Chang (Wu and Chang, 2007). It has been concluded that Si plays a significant role in bone repair and regeneration of bone. Therefore, the in vivo biological performance of the Mg alloy should be enhanced using Si-containing coating (Wang et al., 2015b). In addition, the anticorrosion ability and hemocompatibility of Mg alloy for biomedical application has been significantly improved by MgO coating synthesized using micro-arc oxidation in a multi-step surface modification process. A porous MgO coating as an intermediate layer was prepared on the surface of AZ31 magnesium alloy to the improvement of corrosion resistance (Shi et al., 2015a, 2015b). Brink (Brink, 1997) added MgO to a series of bioactive glasses to maintain bioactivity. Some in vitro results actually indicate that MgO has a detrimental effect on apatite formation (Ebisawa et al., 1990; Kasuga et al., 1987; Watts et al., 2010). Furthermore, (Oliveira et al., 2000) claimed that MgO has a beneficial effect as it improves the early stages of mineralization and contributes to intimate contact with living tissue.

In present study, a powder metallurgy technique consisting of ball milling–multi step cold pressing and subsequent sintering used for fabrication monolayer MgO and double-layer Si/MgO coatings on the surface of Mg/15 wt%TiO_2/5 wt%HA nonocomposite to enhance the corrosion resistance, mechanical integrity and biocompatibility of this nanocomposite for implant applications. Therefore, microstructure, in vitro biocompatibility, mechanical properties, electrochemical and long-term corrosion behavior of uncoated and coated nanocomposites were investigated.

2. Materials and methods

2.1. Preparation of the powder samples of uncoated, MgO-coated and Si/MgO-coated Mg/TiO_2/HA bionanocomposites

2.1.1. Raw materials

Pure magnesium powder (Mg powders, ≥ 99%, 5–20 μm particle size), periclase nanopowders (MgO, 99%, average particle size < 100 nm), hydroxyapatite (HA nanopowder ≥ 97%, < 100 nm particle size), and pure Si (99%, sieve size of 325 mesh) powders under SIGMA-ALDRICH brand used as the raw materials.

2.1.2. Preparation of the uncoated Mg/TiO_2/HA bionanocomposites

A vacuum dry oven used to dry the raw material and the coating powders (Si powders and MgO with flake-like morphology) at 220 °C for 10 h. A subsequent mixing by a planetary ball mill was performed on the 80 wt% Mg, 5 wt% HA and 15 wt% TiO_2 powders in an inert gas atmosphere for 2 h. A uniaxial press at ~840 MPa pressure used to fabricate of cylindrical pellets (Ø12 mm × 5 mm) of uncoated Mg/15TiO_2/5HA bionanocomposites from ball-milled powders. Subsequently, the pellets sintered for 2 h at ~400 °C in a tube furnace under argon atmosphere to finish the fabrication process of compact bare specimens.

2.1.3. Preparation of the MgO-coated Mg/TiO_2/HA bionanocomposites

For preparation of MgO-coated samples, the ball milled powders of Mg, HA and TiO_2 mixture pressed at pressure ~460 MPa in first stage of cold pressing. Then as illustrated in Fig. 1, the upper punch exited from the steel die and a specific amount of MgO powders (consisted of sheet-like particles) decanted on the surface of cold-pressed nanocomposite inside the die. After decanting the MgO powders on the surface of pressed sample that were inside the steel die, a vibration system used to homogenize the thickness of MgO powders in different places of surface of the pressed nanocomposite. In next stage, cold pressing was applied at ~815 MPa to assemble of MgO coating on the surface of Mg/TiO_2/HA nanocomposite. The amount of added MgO in steel die was determined by repeating the experiments, SEM microscopy observations of thickness of MgO coating, density measurements and the coating adhesion measurements to obtain the acceptable adhesion strength of fabricated MgO coating layer with substrate. The minimum required value for the adhesion strength of coatings to the implants is 22 MPa, according to ASTM1147-F (Shi et al., 2015a, 2015b). In last stage, the MgO-coated sample sintered for 1.5 h under argon atmosphere.

2.1.4. Preparation of the Si/MgO-coated Mg/TiO_2/HA bionanocomposites

In the case double layer Si/MgO coating, the cold pressing performed at 340 MPa to press ball-milled Mg/TiO_2/HA powders and 570 MPa pressure was applied to fabricate MgO layer on the surface of cold-pressed Mg/TiO_2/HA in first and second stages of pressing, respectively. In the third step, the specific amount of Si powders decanted on the surface MgO-coated sample into the die, the thickness of Si layer homogenized in different parts of surface using vibration system, and then the powder system pressed under around 800 MPa pressure. As reported in MgO coating process, the amount of Si powder for coating was determined by repeating coating process to obtain the fabricated coatings with good adhesion strength to substrate that is very important factor to protect Mg-substrate implants against corrosive solution. Finally, the Si/MgO-coated nanocomposite sintered 2 h at 540 °C under argon atmosphere for densification of powder sample and better adhesion coating to the substrate. The characterization, corrosion investigations, mechanical analysis and biological tests performed on these sintered pellets. The relative density (=measured density/theoretical density) of the sintered pellets considered as an important parameter to determine the cold pressing and sintering condition, as the minimum ratio of relative density was 85% to carry out a reasonable comparison in corrosion resistance, mechanical characteristics and cytotoxicity uncoated and coated Mg/TiO_2/HA bionanocomposites.

2.2. Characterization of the powder samples of uncoated, MgO-coated and Si/MgO-coated Mg/TiO_2/HA bionanocomposites

The surface and cross-sectional morphologies of the coatings, as well as the corrosion products were observed using a field-emission scanning electron microscopy (FE-SEM) and a transmission electron microscopy (TEM). The crystal structure, phase evolution and chemical

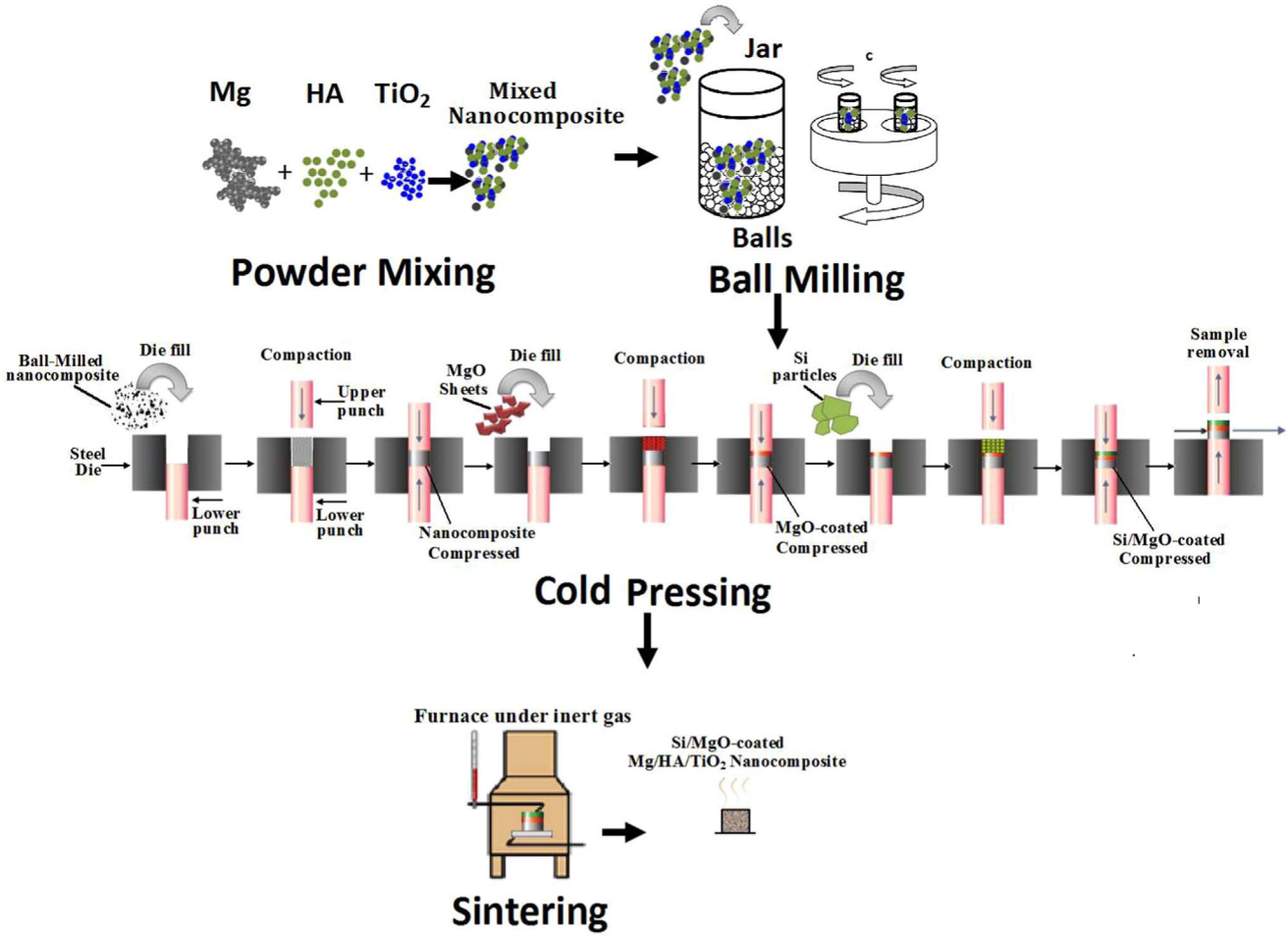

Fig. 1. A schematic image of ball milling-multi step cold pressing-sintering powder metallurgy process to fabricate MgO-coated and Si/MgO-coated Mg/TiO_2/HA Bionanocomposite.

compositions of uncoated, MgO-coated and Si/MgO-coated Mg/TiO_2/HA bionanocomposites and corrosion products were characterized by X-ray diffraction (XRD), energy dispersive X-ray spectroscopy (EDS) and X-ray photoelectron spectroscopy (XPS). Water contact angles to examine surface wettability of uncoated and coated samples were observed with a video based optical contact angle measurement system. Coating bonding measurements were carried out by pull-off test using a portable adhesion tester according to standard test method ASTM D4541 (Amiri et al., 2017).

2.3. Electrochemical tests

Versastat3 potentiostat/galvanostat machine used to record the electrochemical test at 37 °C by a glass cell (containing 250 ml of Kokubo simulated body fluid (SBF) at a pH ~7.56). The details of this test are similar with, which were reported in our previous studies (khalajabadi et al., 2017, 2016, 2015).

This machine also used to measure the electrochemical impedance spectra (EIS) were measured over a frequency range of 1 Hz to100 kHz. The reproducibility of the results was confirmed by repeating each electrochemical test.

2.4. Immersion tests

The volume hydrogen gas released from the samples measured by socking the samples in SBF solution for 168 h. A sample was immersed in a beaker that was covered with a funnel covered the immersed sample to collect the evolved hydrogen gas in a burette that is fixed above the funnel. Prior to renewing the solution, the volume of the released hydrogen gas was calculated in ml/cm^2 as well as a scaled burette used to measure the hydrogen volume.

After an interval of 24 h, the average value of pH of the SBF was recorded from five measurements during the immersion experiment. After different intervals of soaking, a Benchtop pH-meter used for measuring the pH of the SBF solution. Immersed tests performed on the coated samples that only their coated surfaces are in contact with the SBF and the surface sides are sealed.

2.5. In vitro biological tests

The seventh passage of the normal human osteoblasts (NHOst) cells cultured in an osteoblast basal medium (OBM) with the osteoblast growth medium (OGM), which was supplemented with 0.1% ascorbic acid, 10% Fetal Bovine Serum (FBS) and 0.1% of gentamycin was used to investigate ell viability. Indirect contact was used to perform the cell viability test using the MTT (3-(4, 5-Dimethylthiazol-2-yl)-2,5-Diphenyltetrazolium Bromide) assay (Invitrogen, M6494)); 1.5×10^4 NHOst cells were seeded in each well of a 96-well plate for 24 h, and the media were then replaced with the sample extracts after 3, 7 and 9 days. For the MTT-assay, triplicates were performed, and the percentage of cell viability can be calculated using the formula as follows:

$$Cell Viability(\%) = \frac{ODsample - ODblank}{ODcontrol - ODblank} \times 100\% \quad (1)$$

where OD means the optical density (Pan et al., 2016).

The 12-well culture plates were used to place the sterilized disks of uncoated, MgO-coated and Si/MgO-coated Mg/TiO_2/HA bionanocomposites to determine the cell adhesions then 5.2×10^4 osteoblast

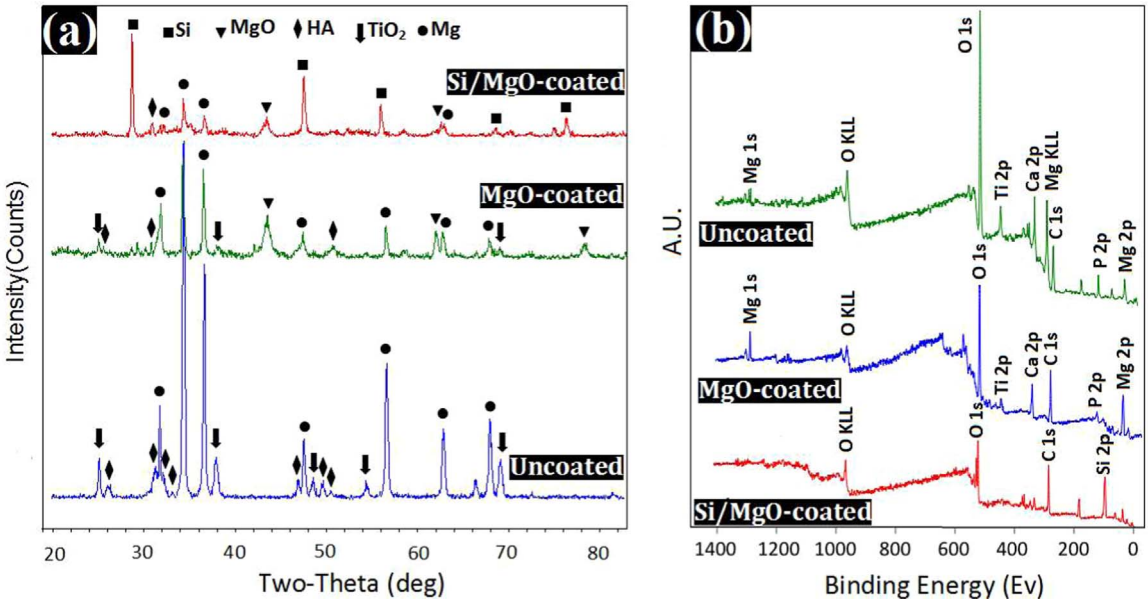

Fig. 2. (a) XRD patterns and (b) Survey XPS spectra of the uncoated, MgO-coated and Si/MgO-coated Mg/TiO_2/HA bionanocomposites after the ball milling-cold pressing-sintering PM process.

cells were seeded in each of the disks. The gold coating was deposited on the surface dried samples before the investigation the adhesion and morphology of the osteoblast cells by a field-emission scanning electron microscopy

The dried samples were gold coated and. More details about the biological tests could be found in our previous published works (khalajabadi et al., 2017, 2016).

2.6. Compression testing

The compression tests were performed to determine the mechanical properties of as-fabricated uncoated and coated nanocomposites using an INSTRON universal testing machine at 50 kN load cell and crosshead speed of 0.5 mm/min. Based on the (ASTM E9-09, 2009) standard, the ratio of height to diameter of samples was determined at one. By occurrence a dramatic decrease in compression load (> 20% load), the mechanical tests were laid off. A surface layer with one mm of thickness, which was in direct contact with the upper punch of die during PM process of fabrication samples was machined off from the uncoated and coated samples, to study the influence of the microstructural defects at the edges of the fabricated samples on the strength and failure strain of nanocomposites. Then, the compression test was carried out on the machined samples under the similar condition.

3. Results and discussion

3.1. Microstructure, chemical composition and phase analysis

3.1.1. XRD analysis

The XRD pattern of the Mg/15TiO_2/5HA (Fig. 2a) nanocomposite indicates the substrate is composed of Mg, TiO_2 and HA phases. Fig. 2a shows the MgO-coated sample mainly consisted of MgO, Mg, and TiO_2. The strong Mg and TiO_2 peaks are due to the substrate; however, the small spectra of HA almost were not detected. With regards the XRD patterns, the main compound residing on the Si/MgO double layer coatings is Si. The intensity of XRD peaks of Mg and TiO_2 are significantly decreased and some of them disappeared that can be caused by the thickness of double-layer coating.

3.1.2. XPS analysis

To understand the surface chemical composition of uncoated and coated samples, the outer surface of samples was examined by XPS. It is known that this analysis is especially used for the surface. Fig. 2b shows the overview XPS spectra of uncoated sample, MgO and Si/MgO coatings. As can be seen, O, C, Mg, Ti, Ca and P elements are detected on the surface of uncoated Mg/TiO_2/HA nanocomposite (Fig. 2b). Ca 2p, P 2p and O 1s peaks at 352 eV, 138 eV and 532 eV, respectively, correspond to the HA; however, TiO_2 in substrate of nanocomposite is presented by Ti 2p (Qi et al., 2008) and O 1s spectra at 458 eV and 532 eV, respectively. The scan analysis of Mg 1s at approximately 1304 eV revealed a peak that can be belonged to metallic state of Mg from the substrate of nanocomposite and/or assigned to MgO (Chen et al., 2015; Jin et al., 2015; Khalajabadi et al., 2016). The signal of Mg 2s at ~88.5 eV should come from the magnesium of nanocomposite substrate (Gu et al., 2016). After assembling of porous MgO coating on the nanocomposite surface by PM route, the intensity of Ca 2p, P 2p, O 1s, and Ti 2p peaks is decreased, whereas, the height of Mg 1s and Mg 2p spectra at binding energies (BE) of 50.5 eV and 1304 eV, respectively, are raised that confirm the presence MgO layer in outer surface of MgO-coated sample (Li et al., 2017; Wang et al., 2013). The Si 2p signal assigned to Si coating (Li et al., 2013) is observed at 102 eV in the XPS spectrum of double-layered coated sample; however, Mg 2s, Mg 1s, Mg 2p, O 1s, Ca 2p, P 2p, and Ti 2p signals due to Mg, MgO, HA and TiO_2 phases weaken remarkably even disappeared, which attributes to the thickness of Si coating. The existing of binding energy C 1s peak at 286 eV correspond to the carbon can be resulted by the preparation process and keeping the sample in air and/or washing it by acetone before conducting the test (Li et al., 2013; Wang et al., 2013). Mg 1s at approximately 1304 eV may be assigned to the surface magnesium exists in the form of oxidized state, indicating the formation MgO (Chen et al., 2015; Jin et al., 2015). There is no other visible contribution of metallic magnesium related to the main Mg KLL Auger emission peaks. These spectra that were found in the range 304.4–308.8 eV attributed to the oxidation of polycrystalline Mg (Taleatu et al., 2014).

3.1.3. FE-SEM observations and X-ray elemental mapping

FE-SEM images in Fig. 3 show the surface morphologies of bare sample and the coatings that have been assembled by a PM technique. As be seen (Fig. 3a), the large particles with plate-like morphology that uniformly distributed in the layered-microstructure of substrate of bare nanocomposite are surrounded with fine powders. X-ray elemental mapping indicates the Mg particles appear with two types of

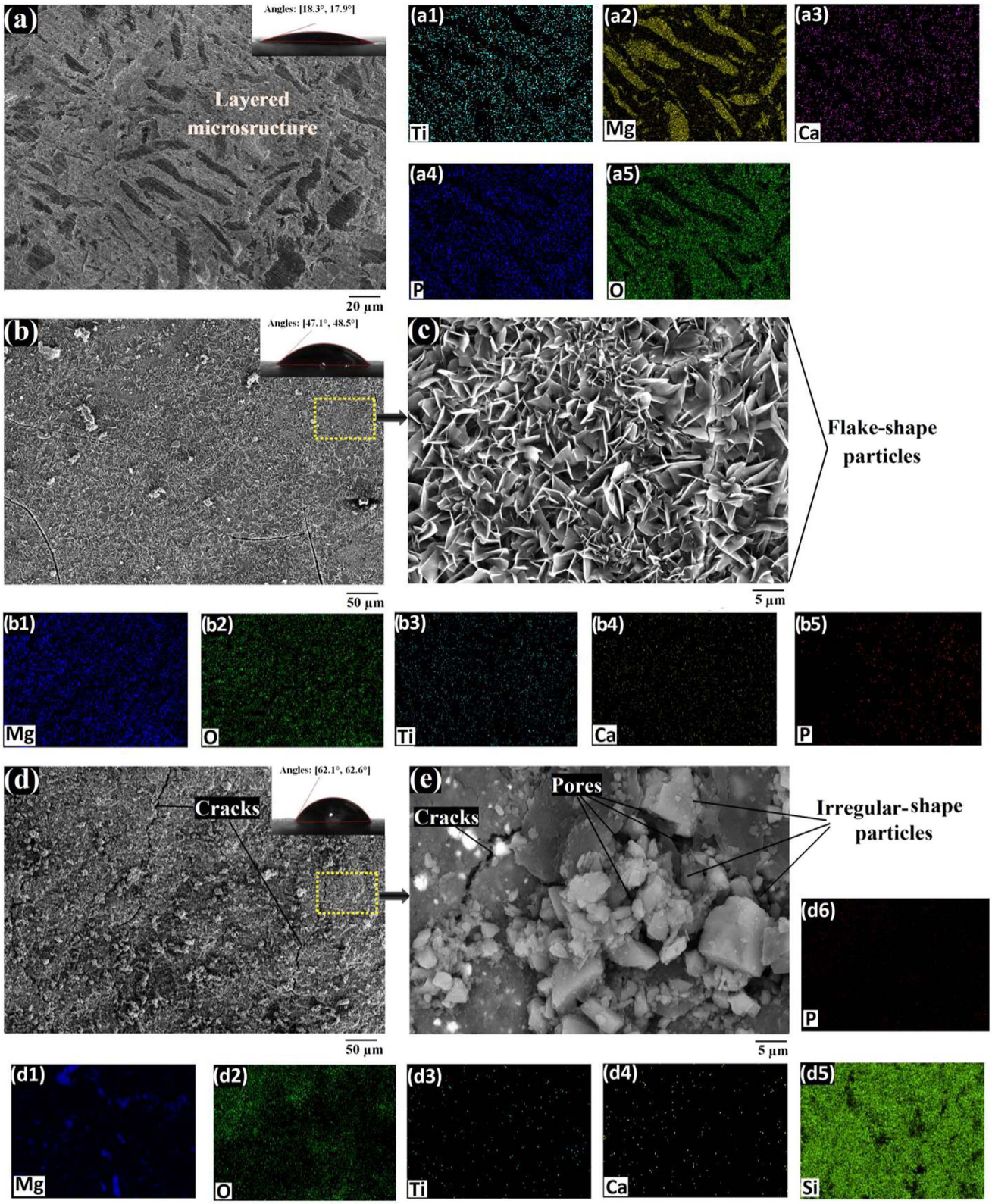

Fig. 3. Surface FE-SEM micrographs of (a) uncoated, (b, c) MgO-coated and (d, e) Si/MgO-coated, X-ray surface elemental mapping of (a1-a5) uncoated, (b1-b5) MgO-coated and (d1-d6) Si/MgO-coated Mg/TiO_2/HA nanocomposites after the ball milling-cold pressing-sintering PM process.

morphology: some of the Mg particles have plate-like morphology, whereas the remainder of the Mg, accompanied with O, Ca, and Ti as fine particles is distributed homogenously among the plates within the powder system of Mg/TiO_2/HA nanocomposite (Fig. 3a1-a5). The surface microstructure of MgO-coated nanocomposite is homogenous and porous comprising the flakes (Fig. 3b and 3c). However, the FE-SEM micrographs depict that a relatively dense and rough layer consisted of irregular-shape particles in micron size covered the outer surface of Si/MgO-coated sample, whereas some porosities and cracks are observed on the coating (Fig. 3d and 3e). X-ray elemental mapping demonstrates

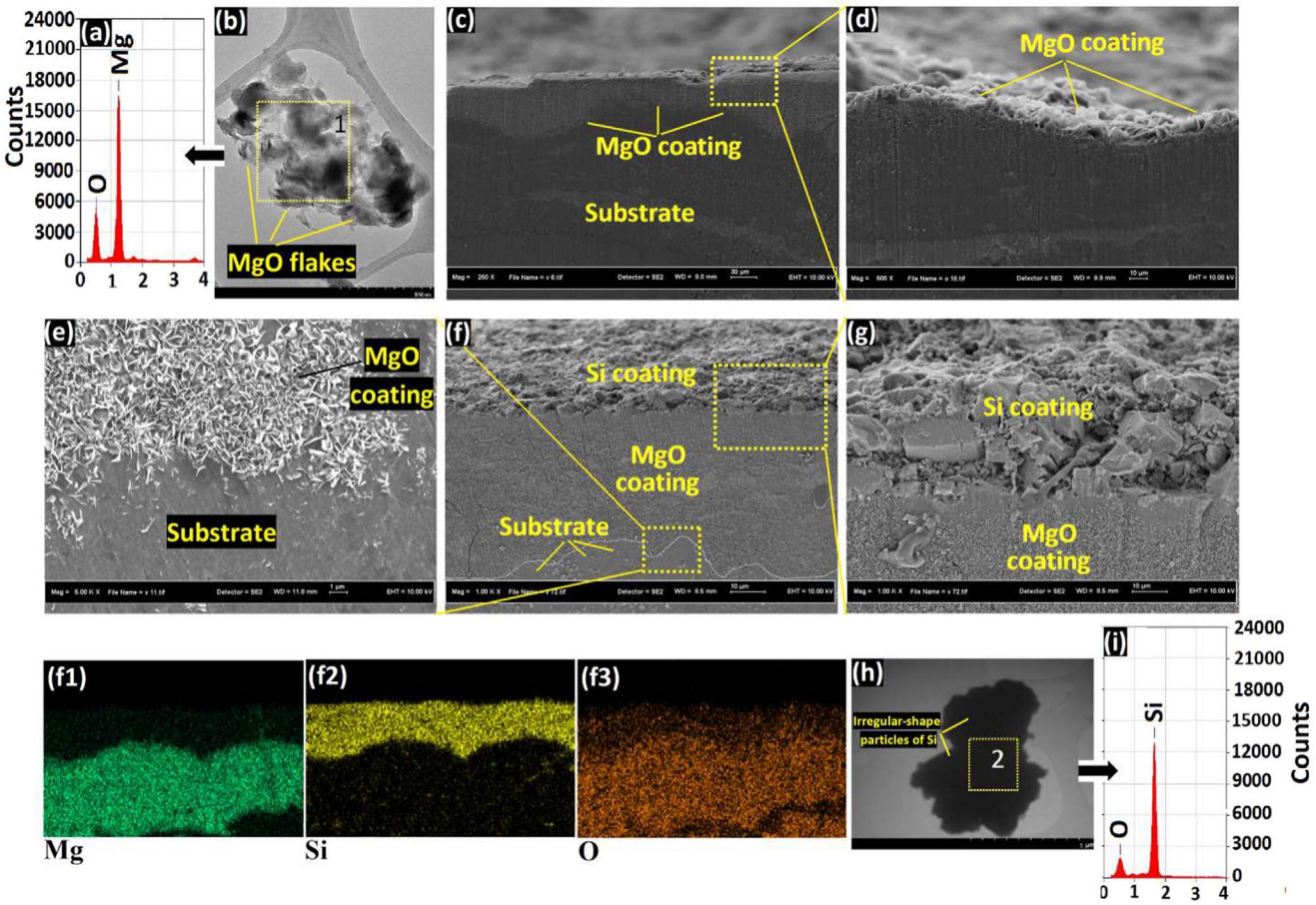

Fig. 4. EDS analyses (a) area 1 and (i) area 2, TEM images of (b) MgO flakes and (h) Si particles, cross-sectional FE-SEM micrographs of (c, d) MgO-coated and (e, f and g) Si/MgO-coated Mg/TiO_2/HA nanocomposites, and (f1-f3) X-ray elemental mapping of Fig. 4f.

the presence of MgO and Si layers in outer surface of MgO-coated and Si/MgO-coated samples. Fig. 4 presents the cross sectional images of the mono- and double-layered coated nanocomposites. The single-layer MgO coating with 46 μm of average thickness that composed of MgO flakes is porous (light gray color) without any discontinuity in interface between the coating and substrate with dark gray color. However, the double layer coating consisting of an inner layer of flake-like particles of MgO with well-dispersed porosities as well as the densely packed outer layer on the surface of double-layered Si/MgO-coated nanocomposite formed by the Si particles with irregular shape. The average coating thickness of double-layer Si/MgO is measured 67 μm: the thickness of inner layer is around 44 μm; however, the average thickness of outer coverage is obtained 23 μm. The fair uniformity of the morphology and thickness of the coatings; moreover, the adhesion of coatings to the substrate (after serious grinding) are also confirmed by the cross-sectional micrographs. Furthermore, the X-ray elemental mapping of double layer Si/MgO coting (Fig. 4f1-f3 related to the Fig. 4) confirm the fabrication and thickness uniformity of coatings as Si showed by yellow color in outer layer of coating, whereas Mg and O in inner side of coating are illustrated by green and brown colors, respectively.

3.1.4. TEM observations

The TEM images depict the morphology of MgO flakes (Fig. 4a and b) and irregular-shape particles of Si accompanied with their EDS analysis (Fig. 4h and i). The TEM-EDX pattern exhibits only the presence of Mg and O as elemental composition that ensures the chemical purity of the MgO flake-like powders.

3.1.5. Bonding strength measurements

In order to evaluate the bonding strength of the mono and double layer coatings, the pull-off test was performed on the coated samples. The bonding strength of the monolayer MgO coating is measured 35.6 ± 1.2 MPa, whereas by fabrication of Si as a second coating layer the bonding strength of double layer Si/MgO coating decreased to 31.4 ± 2.7 MPa. This might happen as a result of increasing the thickness of coating, more agglomerated particles in the outer surface of coating and/or less uniformity. Preparation a homogenous coating with micron-size thickness by good adhesion strength to the substrate using a low price and facile method could be a significant improvement for surface modification of magnesium powder alloys.

3.2. Electrochemical corrosion tests and immersion behavior

3.2.1. EIS test

The ability of a coating to protect the substrate can evaluate by electrochemical impedance spectroscopy (EIS) as a useful technology way. Fig. 5 shows the Nyquist plots (Fig. 5b) and the Bode plots (Fig. 5a and 5c) for the bare, MgO-coated and Si/MgO-coated samples in SBF solution. The differences in the diameter size of capacitive Nyquist loops for uncoated and coated nanocomposites can attribute to the charge transfer resistance of the corrosion process (Fig. 5b). It discloses that the Si/MgO-coated sample presents an overall largest constant loop among all the samples. The diameter of the capacitive loop indicates the anticorrosion property (Chang et al., 2007; Zhang et al., 2016b), evidencing that the Si/MgO coating provides a more effective barrier effect against corrosive solution. According to the illustrated models in Fig. 5d, one R_2–CPE_2-circuit was used by fitting the simplified equivalent electrical circuit (EEC) with the spectrum of the uncoated sample

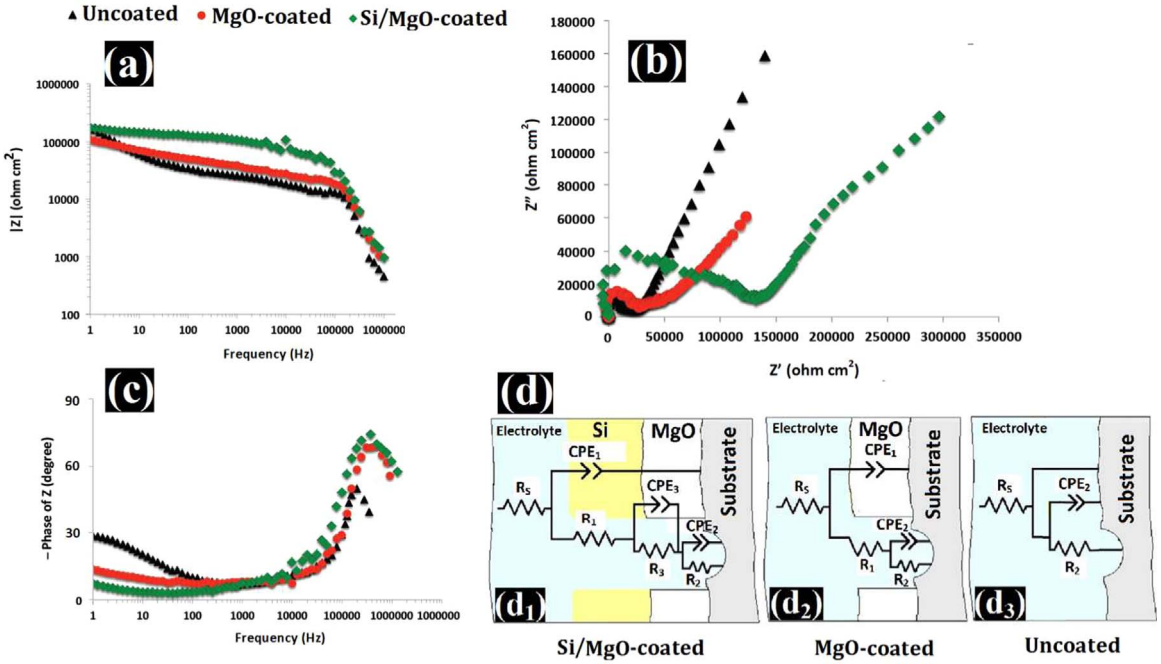

Fig. 5. Bode plots (a) impedance modulus vs. frequency plots and (c) phase angle vs. frequency plots for the uncoated, (b) Nyquist plots of MgO-coated, and Si/MgO-coated Mg/TiO_2/HA nanocomposites in SBF solution and (d) The models for the coatings structure and the appropriate equivalent electrical circuits, used for experimental impedance data fitting ((d_1) with three *R-CPE* circuits, (d_2) with two *R-CPE* circuits and (d_3) with one *R-CPE* circuit).

(Fig. 5d_3), where R_2 is the charge transfer resistance, CPE_2 is the double layer capacitance and R_S represents the solution resistance. In the allocated circuit of MgO coated sample, the R_1–CPE_1 elements describe the MgO coating, as well as the R_2-CPE_2 elements are related to the substrate (Fig. 5d_2). Meanwhile, the diameter of the capacitive loop related to the MgO-coated sample increased compared to that of the uncoated one, which indicates the enhancement the anticorrosive characteristics of the Mg/TiO_2/HA nanocomposite in the SBF electrolyte by mono-layer Si coating. The EEC with three *R–CPE*-circuits was used to fit the experimental impedance spectra for calculation the quantitative parameters of the EEC elements, which characterize the coverage MgO and Si layers (Fig. 5d). The third time constant (R_3–CPE_3) is arisen by the MgO intermediate layer. The presented three-*R-CPE*-circuit EES indicates the double-layered Si/MgO-coated nanocomposite under examination. The electrochemical resistance (R_e) regarded as measure of corrosion resistance is calculated by adding R_1, R_2 and R_3. The R_e values of the MgO-coated, the Si/MgO-coated samples are larger than that of the bare Mg/TiO_2/HA nanocomposite, which indicates the protection of the two kinds of coatings for the substrate. The R_e of the MgO-coated sample (31.5 kΩ cm^2) was nearly 4 orders of magnitude larger than that of the uncoated sample (16.4 kΩ cm^2), showing the porous MgO coverage could improve the corrosion resistance of the Mg/HA/TiO_2 nanocomposite, which can be attributed to the different corrosion behavior and microstructure of the MgO coating. Furthermore, the value of electrochemical resistance of Si/MgO-coated sample ($R_{e=128.6}$ kΩ.cm^2) measured close to 8 times of magnitude higher than that of the uncoated sample. Such an improvement should come from two aspects: On one hand, the different electrochemical properties of Si as a top layer compared with that of the substrate may improve the corrosion resistance of Si/MgO-coated sample. On the other hand, fabrication Si layer can increase the thickness of coating, cover the presented porosities on the surface of MgO coating and as a result improve the protection of magnesium-based composite substrate against the corrosive environment. Additionally, the microstructural imperfections of the Si coating comprising micron size particles enlarge its exposure area immersed in the corrosive medium, the micro pores and cracks act as the passages for the corrosive Cl^- penetrating into the Si coating to the substrate. However, the presence of MgO as a sub layer in double-layer Si/MgO coating with thickness ~67 μm can restrict the penetration of SBF in substrate. As can be seen in Fig. 5b, the diffusion control mechanism Warburg impedance indicated by the emergence a tail in the Nyquist plots of samples. When the counter ions moved through the surface, Warburg behavior is taken place, which indicates the slower occurrence of diffusion process than the metal charge-transfer reaction, and as a result, a diffusion barrier mechanism is developed in the surface against the corrosion attack (Chen et al., 2012; Gu et al., 2013; Ryu et al., 2012). As shown in Bode plots (Fig. 5a), at low frequency region (100–1000 Hz), the initial modulus value for MgO-coated and Si/MgO-coated samples is higher than that of the bare nanocomposite. The higher impedance difference between the high and the low frequency means the better corrosion resistance is provided (Zhang et al., 2016b). The increase of the modulus value for the coating with MgO layer, indicating the existence of the porous MgO layer enhanced the corrosion resistance of the nanocomposite substrate. Furthermore, the Si/MgO-coated sample possessed the highest impedance modulus, compared with the bare and MgO-coated sample. It reveals that thick Si/MgO coating facilitated an excellent corrosion resistance for Mg/15TiO_2/5HA substrate attributed to protection by double layer Si/MgO coating. This speculation is clearly reflected by the lower phase angle of Si/MgO (76°) compared to only MgO coating (68°) and the bare (51°) nanocomposite. For the Si/MgO-coated sample, the curves in Bode plots (Fig. 5c) reveal the time constants (the peak at min degree of phase angle) at frequencies of 383 kHz, 342 kHz and 205 kHz for Si/MgO-coated, MgO-coated and uncoated samples, respectively. The presence of the time constant at a higher frequency and lower phase angle is attributed to the Si/MgO coating property, suggesting it possesses a fine physical barrier to the corrosive media. The results of Nyquist diagram are consistent with those obtained through the Bode diagram and are also supported by the plot of the phase angle and impedance versus frequency.

3.2.2. Potentiodynamic polarization test

Fig. 6 shows the potentiodynamic polarization curves of MgO-coated, Si/MgO-coated and uncoated nanocomposites in SBF aqueous

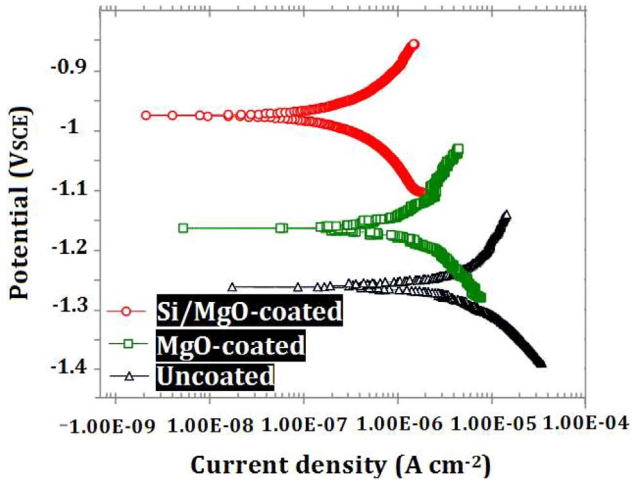

Fig. 6. Potentiodynamic polarization curves of uncoated, MgO-coated and Si/MgO-coated Mg/TiO_2/HA nanocomposites in SBF solution.

solution. For magnesium and its alloys, the cathodic polarization curve generally represent the cathodic hydrogen evolution by water reduction, as well as the anodic one is considered to represent dissolution of magnesium or corrosion behaviors of the surface protective layer.

The anodic and cathodic reactions can be written as follows:

$$Mg \rightarrow Mg^{+2} + 2e^{-} \text{ Anodic reaction} \quad (2)$$

$$2H_2O + 2e^{-} \rightarrow H_2 + 2OH^{-} \text{ Cathodic reaction} \quad (3)$$

The corrosion current density (*i*corr), corrosion potential (*Ecorr, VSCE*), cathodic Tafel slopes (βc), anodic Tafel slopes (βa) and corresponding corrosion rate (*P*i) of the specimens extracted from the polarization curves are listed in Table 1. As can be observed in Fig. 6 and Table 1, the lower polarization current densities were obtained for the coated samples than that of the uncoated one. The polarization current density of nanocomposite coated by MgO (2.7 μA/cm^2) is less compared to the case of the bare sample (4.8 μA/cm^2), indicating the MgO coating declined the corrosion rate of nanocomposite. Based on Eq. (4), the corrosion rate (P_i) of magnesium-based composites can be calculated using the corrosion current density, i_{corr} (mA/cm^2) as follows (Shi et al., 2010; Zhao et al., 2008, 2009):

$$P_i = 22.85 i_{corr} \quad (4)$$

It is evident that the corrosion current density (i_{corr}) decreased gradually from 2.8 μA in MgO-coated sample to 0.89 μA for Si/MgO-coated sample. The Si/MgO-coated nanocomposite shows the lowest corrosion rate (0.02 mm/year) among the uncoated (0.10 mm/year) and coated samples (0.06 mm/year). In addition, another important finding from the polarization curves is the corrosion potential (E_{corr}) that MgO and Si/MgO coatings led to a significant change in its value in the SBF solution. As shown in Table 1, the Si/MgO-coated sample depicts the most positive E_{corr} compared with the bare and MgO-coated sample. The less noble E_{corr} was obtained for the MgO coated layer compared with the E_{corr} of uncoated nanocomposite. The nobler E_{corr} means the sample is more stable thermodynamically, meanwhile, the lower i_{corr} means slower corrosion process in kinetics (Choi and Kim, 2016). Additionally, the polarization resistance (R_P) of the bare and coated samples can be calculated using the electrochemical parameters (*i*corr, βa and βc) tafel plots in Eq. (5) (Wang et al., 2015a; Zhao et al., 2010) as follows:

$$Rp = \frac{\beta a \beta c}{2.3(\beta a + \beta c) i_{corr}} \quad (5)$$

The results indicate that the polarization resistance improved from 11.86 kΩ cm^2 for uncoated Mg/TiO_2/HA nanocomposite to 67.36 kΩ cm^2. Moreover, the MgO-coated sample corrodes with much larger polarization resistance (21.28 kΩ cm^2) than that of the bare sample.

3.2.3. Immersion tests

Furthermore, the long-term in vitro immersion tests were undertaken to evaluate the long-term corrosion behavior of the Si/MgO-coated, MgO-coated and uncoated Mg/TiO_2/HA nanocomposites. The hydrogen evolution and the increased pH value of SBF solution basically reflect the corrosion rate and are usually measured as the indicators of the magnesium degradation rate (Pan et al., 2016). It is well known that the overall corrosion reaction of magnesium in aqueous solution at its corrosion potential can be expressed as follows:

$$Mg + 2H_2O \rightarrow Mg^{2+} + 2OH^{-} + H_2\uparrow \quad (6)$$

As a consequence, Mg-based nanocomposite reacts with H_2O so that the degradation of magnesium leads to an increase of the pH value in the surrounding area (Han et al., 2016). Fig. 7a illustrates the pH variation value of SBF solution at different immersion times. During the early stages of medical application of biodegradable implants, the corrosion rate plays a critical role in the initial surrounding tissue response. Very fast initial degradation rate of implants lead to occurrence of osteolysis, which affect adversely the regeneration of bone tissue (Guan et al., 2012). Therefore, the reduction of initial degradation rate of Mg-based nanocomposite is very important issue for their implant applications. It can be seen (Fig. 7a), the pH value increased by increasing immersion time for all the samples. The pH increase of uncoated sample occurred by a faster rate compared to the MgO coating specimen. At the first day, the pH value increased almost sharply for uncoated sample due to the increase of OH^- concentration of SBF solution caused by the release of Mg^{2+} according to the reactions of (3) and (6) (Atrens et al., 2011; Yang et al., 2016). The pH of solution surrounding the uncoated sample increased from 7.46 to 8 while only about 0.05–0.15 increases was observed in the pH of coated samples, which can be related to the presence protective MgO and Si/MgO coatings. This result is consistent with the observation of hydrogen bubbles. By increasing of immersion time from 24 h to longer times, the pH value of coated samples increased with a higher rate that can be caused by the breakdown of coating layers in some parts and penetration of SBF solution into the substrate of nanocomposite. At longer immersion time after 2 or 3–4 or 5 days, the changes of pH value for all immersion solution slow down by deposition of corrosion products on the surface of samples that hinder more degradation of substrate; additionally, the formation of $Mg(OH)_2$ and HA according to the reactions (7), (9) and (10) consumes OH^- ions of SBF and as a result stabilizes the pH values. This result could be attributed to high pH value and the presence of HCO^{3-}, HPO_4^{2-}, Mg^{2+} and Ca^{2+} in SBF can improve the

Table 1
Electrochemical parameters of the uncoated and MgO- and Si/MgO-coated Mg/TiO_2/HA nanocomposites in SBF solution attained from the polarization test.

Sample	Corrosion potential, E_{corr} (mV vs. SCE)	Current density, i_{corr} (μA/cm^2)	Cathodic slope, βc (mV/decade) vs. SCE	Anodic slope, βa (mV/decade) vs. SCE	Polarization resistance, R_P (kΩ cm^2)	Corrosion rate, *Pi* (mm/year)
Uncoated	−1255.7	4.8	193.7	404.6	11.86	0.10
MgO -coated	−1156.2	2.7	235.5	342.1	21.28	0.06
Si/MgO-coated	−970.8	0.85	208.51	407.2	67.36	0.02

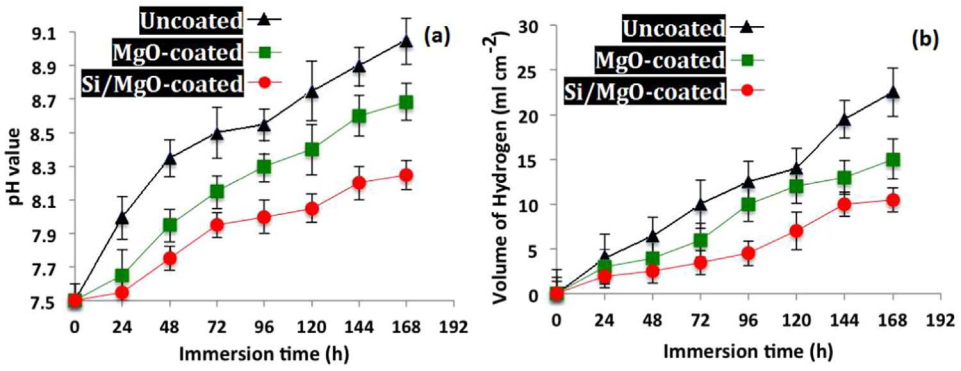

Fig. 7. (a) Change in pH of the SBF solution and (b) Hydrogen evolution during immersion of uncoated, MgO-coated and Si/MgO-coated Mg/TiO_2/HA nanocomposites for duration of 168 h.

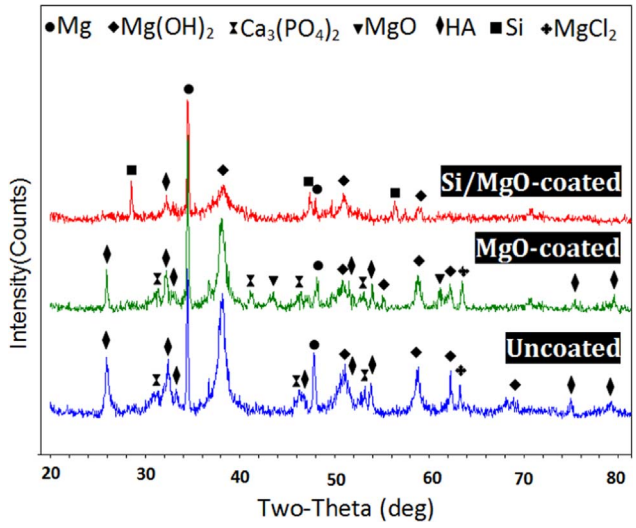

Fig. 8. XRD patterns of uncoated, MgO-coated and Si/MgO-coated specimens after 14 days of immersion in a SBF solution at 37 °C.

precipitation of CaP components on the surface of samples as a barrier to protect samples against the corrosive medium. Furthermore, with increasing immersion time from 4 or 5 days to 7 days, the slope of pH values of sample was gradually ascended, which is probably caused by the breaking and dissolution of the corrosion product layers. However, the pH value of Si/MgO coating reaches about 8.2 later and remains stable for the rest of the immersion days, the pH values of MgO coating shows a smaller increase compared to the occurred increase in pH value of uncoated sample. After 7 days immersion, the highest change observed in the pH value of surrounding solution of uncoated sample as the pH value reached to about 9, whereas the pH values of the SBF solution of MgO-coated and Si/MgO-coated immersed samples are around 8.7 and 8.2, respectively. It can be seen that the pH value of surrounding solution of the MgO and Si/MgO coatings is obviously lower than that of the bare substrate at all time points. Moreover, the measured pH value of the Si/MgO-coated sample is lower than those of the MgO-coated. Therefore, the better degradation resistances can be resulted for the coated samples with single-layered MgO and double-layered Si/MgO than that of the uncoated sample (Yang et al., 2016). Fig. 7b depicts the cumulative hydrogen gas evolution plots illustrated for the uncoated, MgO-coated and Si/MgO-coated samples. The cumulative hydrogen amount released from the bare Mg/TiO_2/HA nanocomposite is higher compared with that of the MgO and Si/MgO coatings. During the immersion, the lowest hydrogen evolution amount was measured for the Si/MgO double-layered coated sample. This described the un-coated and MgO-coated nanocomposites undergone severer corrosion in the SBF. However, dual-layered Si/MgO coating could effectively inhibit the degradation of un-coated sample. In addition, it can be observed that the degradation rate amplified after 168 h from 22.5 ml/cm^2 in uncoated sample to 15 ml/cm^2 for the single-layered MgO coated sample, respectively. The results indicate that dual-layered Si/MgO coating remarkably suppressed the hydrogen evolution (10.5 ml/cm^2) over the long immersion period, considerably lower compared to all the other samples. With regards the EIS, polarization and log-term immersion tests, the presence of MgO and Si coatings on the surface of Mg/TiO_2/HA nanocomposite effectively increased the degradation resistance of substrate. It can be caused by the decrease of contact area between the corrosive solution and the substrate (consisting magnesium) due to the presence of coating layers of MgO and Si. Additionally, by assemble of coverage layers on the surface of Mg/TiO_2/HA nanocomposite, the wettability of samples declined as indicated by the contact angle measurements (Fig. 3), which led to lower amount of SBF penetrates in the substrate and as a result the degradation rate of samples is restricted. According to the electrochemical corrosion tests and immersion tests, the single-layer MgO coating alone is not good enough to protect the corrosion of Mg-based nanocomposite for a long time period because the MgO coating is porous and also absorbable. Hence, the improvement and sealing of MgO coating by an extra coverage such as Si is required. In order to identify the phases of the corrosion products, XRD was conducted on the surface of the uncoated and coated samples after immersion in the SBF for 14 days, as shown in Fig. 8. It can be found, Mg, $Mg(OH)_2$, HA, $Ca_3(PO_4)_2$ and $MgCl_2$ phases were detected on the surface of uncoated immersed sample. The formation of apatite illustrated the bioactivity of the coating (Kokubo, 1991; Kokubo and Takadama, 2006). It is well known that the overall corrosion reaction of magnesium in aqueous solution at its corrosion potential can be expressed by anodic reaction ($Mg \rightarrow Mg^{2+} + 2e^-$) and cathodic reaction ($2H_2O + 2e^- \rightarrow H\uparrow + 2\,OH^-$). Thus, $Mg(OH)_2$ precipitated in the initial stage of degradation of Mg-based nanocomposites substrate according to the following reaction:

$$Mg^{2+} + 2OH^- \rightarrow Mg(OH)_2 \text{ (product formation)} \quad (7)$$

By increasing the immersion time, the chloride ions (Cl^-) of the SBF solution would react with $Mg(OH)_2$ to form more resoluble $MgCl_2$ phase based on the reaction (7).

$$Mg(OH)_2 + 2Cl^- \rightarrow MgCl_2 + 2OH^- \quad (8)$$

CaP compounds, such as HA and $Ca_3(PO_4)_2$ formed on the surface of the immersed samples due to the reaction of the phosphate ions (HPO_4^{2-} or PO_4^{3-}) and Ca^{2+} with OH^- ions in SBF solution based on the phase transformations (8), (9) and (10) as follows:

$$10Ca^{2+} + 8OH^- + 6HPO_4^{2-} \rightarrow Ca_{10}(PO_4)_6(OH)_2 + 6H_2O \quad (9)$$

$$10Ca^{2+} + 6PO4^{3-} + 2OH^- \rightarrow Ca_{10}(PO_4)_6(OH)_2 \quad (10)$$

$$3Ca^{2+} + 2PO_4^{3-} \rightarrow Ca_3(PO_4)_2 \quad (11)$$

XRD peaks of MgO are detected in X-ray patterns of corrosion products of MgO-coated sample; moreover, despite of the better

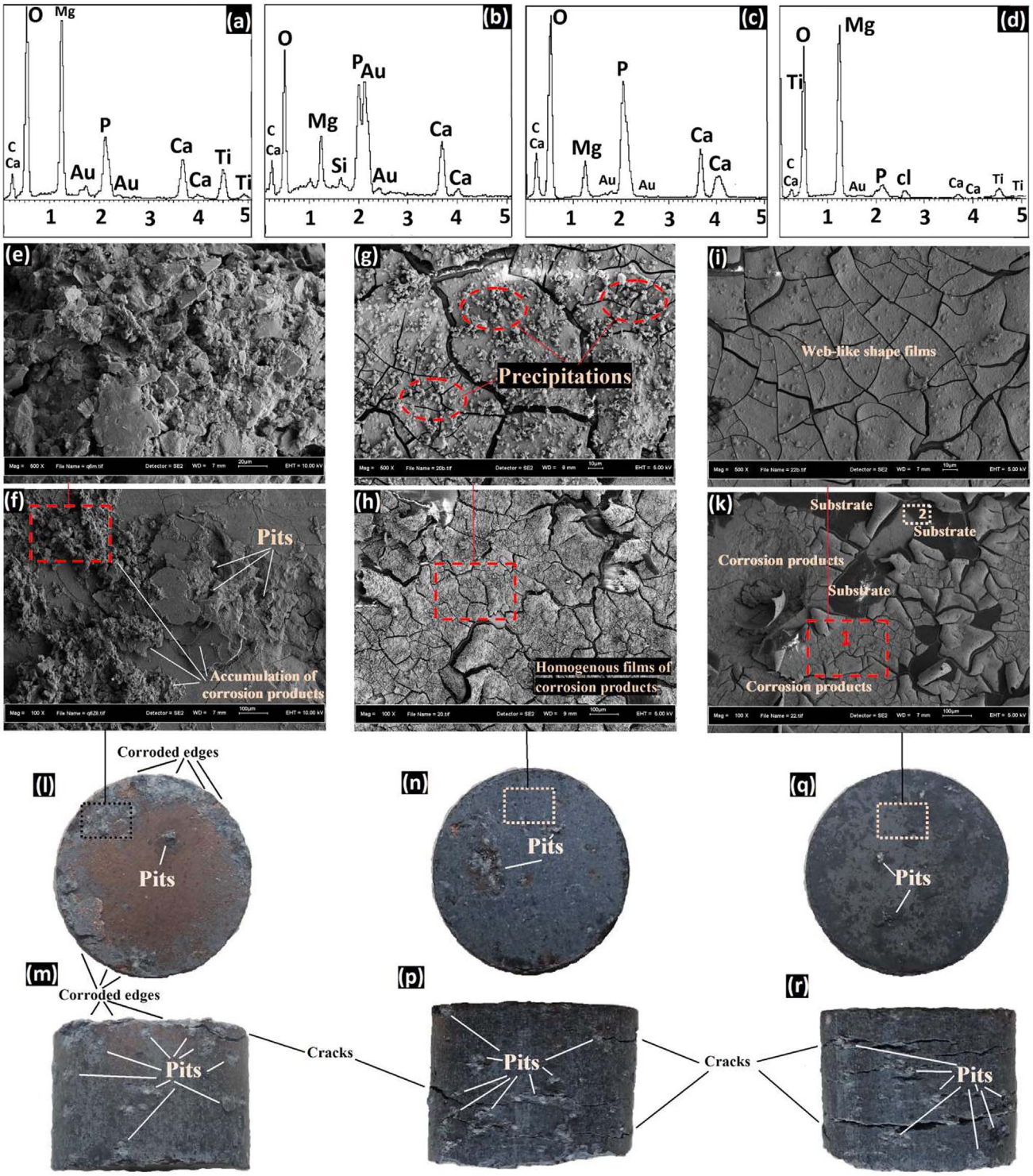

Fig. 9. Surface FE-SEM images of (e, f) uncoated (g and h) MgO-coated and (i, k) Si/MgO coated after 7 days immersion in a SBF solution at 37 °C, EDS analysis (a) image f, (b) image h, (c) area l and (d) area 2, surface and cross-sectional photographs of (l, m) uncoated, (n, p) MgO-coated and (q, r) Si/MgO-coated Mg/TiO_2/HA pellets, after 14 days of immersion in a SBF solution at 37 °C.

corrosion resistance of MgO-coated sample than that of bare sample, the strong peaks of $Mg(OH)_2$ are detected, which can be related to the presence of MgO layer on the outer surface of sample and as a result, formation $Mg(OH)_2$ according to the reaction (12).

$$MgO + H_2O \rightarrow Mg(OH)_2 \quad (12)$$

However, a significant decrease in intensity of the allocated XRD peaks of corrosion products such as $Mg(OH)_2$ and CaP components was observed for Si/MgO-coated sample after 14 days immersion in SBF. Furthermore, XRD spectra of the substrate phases such as Mg, HA and TiO_2 of Mg/TiO_2/HA, as well as coating components (MgO and Si peaks) weaken remarkably even disappear that demonstrates deposition the corrosion products on the surface of immersed Si/MgO-coated sample. It can be described by the precipitation of amorphous phases after immersion in SBF. Fig. 9 exhibits the photographic images of cross-section and side sections of uncoated and coated samples after 14

days immersion in SBF solution. As be seen, the surface of bare sample suffers more serious corrosion attack than the coated ones and as a result, a large amount of the precipitated corrosion products, pits and delamination observed especially on the edges of the sample. FE-SEM micrographs (9e and f) confirm the accumulation of thick corrosion products on the uncoated sample that indicates this sample severely corroded. Precipitation large amount of corrosion products on the surface of bare sample can delay the degradation of sample; however, with increasing the immersion time and progress of degradation, the coverage consisted of corrosion products would be destroyed by intensification of release H_2 gas. With regards the micrograph images, an enhancement in corrosion behavior of Mg/TiO_2/HA nanocomposite coated by MgO is appeared compared to the uncoated sample. As, a homogenous layer consisted of the corrosion products (with bright color) is deposited on the surface of MgO-coated nanocomposite, after 14 days of soaking in SBF solution. Based on the FE-SEM observation, precipitation of a uniform layer of corrosion products on the surface of MgO-coated sample describes the homogenous degradation of this sample with a similar corrosion rate in different parts that can be related to the uniformity of morphology, thickness, and particle size of MgO coating. Additionally, a number of small particles were homogenously deposited on the surface of these layers during immersion in SBF. However, the precipitated products with bright color on the surrounded Si/MgO-coated sample by the SBF are revealed only in some parts, which can describe lower degradation rate of immersed sample. As be seen in Fig. 9i and k, the thin web-like shape films with uniform thickness are deposited on Si/MgO-coated: moreover, smaller amount of spherical particles precipitated on these films that indicates less degradation of this sample rather uncoated and MgO-coated. However, after 14 days of immersion, the side surface of all samples, which are without coverage coatings have almost similar appearance consisting pits and deep cracks that indicates severer corrosion of bare parts of samples compared to the coated surfaces (Fig. 9m, p and r). As can be seen (Fig. 9m, p and r), the pits covered by bright color precipitations that indicate the tendency of deposition of corrosion products in these areas due to the release of OH^- and Mg^{2+} ions by occurrence reactions (6) and (8) then consumption these ions by reactions (7), (9) and (10) to form corrosion products such as $Mg(OH)_2$ and HA. The observation of soaked samples in SBF by photography and FE-SEM confirm the results of the electrochemical corrosion tests and long-term immersion tests. The EDS analysis confirm the XRD results about the deposition $Mg(OH)_2$ and CaP components on the surface of 14 days immersed samples in SBF. The black color parts show the substrate of Si/MgO-coated sample; however, the regions with bright color demonstrate the corrosion products.

3.3. Cell Viability, proliferation and attachment of NHOst osteoblasts

In fact, the ideal biodegradable candidate should have a suitable degradation rate to allow the implant to maintain mechanical support during tissue healing while being nontoxic and compatible to cells (Hornberger et al., 2012; Jin et al., 2015; Shadanbaz and Dias, 2012). The relative cell viability (% of control) of the osteoblast cells (NHOst) was determined after 3, 7 and 9 days of culturing on the uncoated, MgO-coated and Si/MgO-coated Mg/TiO_2/HA nanocomposites by extraction media (Fig. 10e). After 3 days of incubation, the viability of the NHOst cells cultured in the extraction medium of the Si/MgO-coated sample is 74 ± 2%. However, the extracted medium of uncoated nanocomposite, shows significantly reduced cell viability and determined 62 ± 5%. The NHOst cells after incubation with the MgO-coated extraction medium for 3 days display less cell viability (68 ± 3%) compared to that of the Si/MgO-coated sample. However, in comparison with the uncoated nanocomposite, the MgO-coated nanocomposite shows better biocompatibility. It is known that Mg alloys without any surface modification will be seriously degraded in contact with the medium. The degradation process is followed by the production of hydrogen, Mg^{2+} and OH^-, which in turn raise the concentration of Mg ions and the pH value of the medium. Rapid degradation of Mg-based alloys accompanied with the release of hydrogen bubbles is detrimental to the cell culture and prevents the survival and proliferation of cultured cells. As the cells would be pushed away from the substrate surface by the continuous release H_2, which inhibits the cell adhesion on the sample surfaces in vitro and in vivo. As cells are very sensitive to environmental fluctuations, MgO and Si/MgO coatings provided an

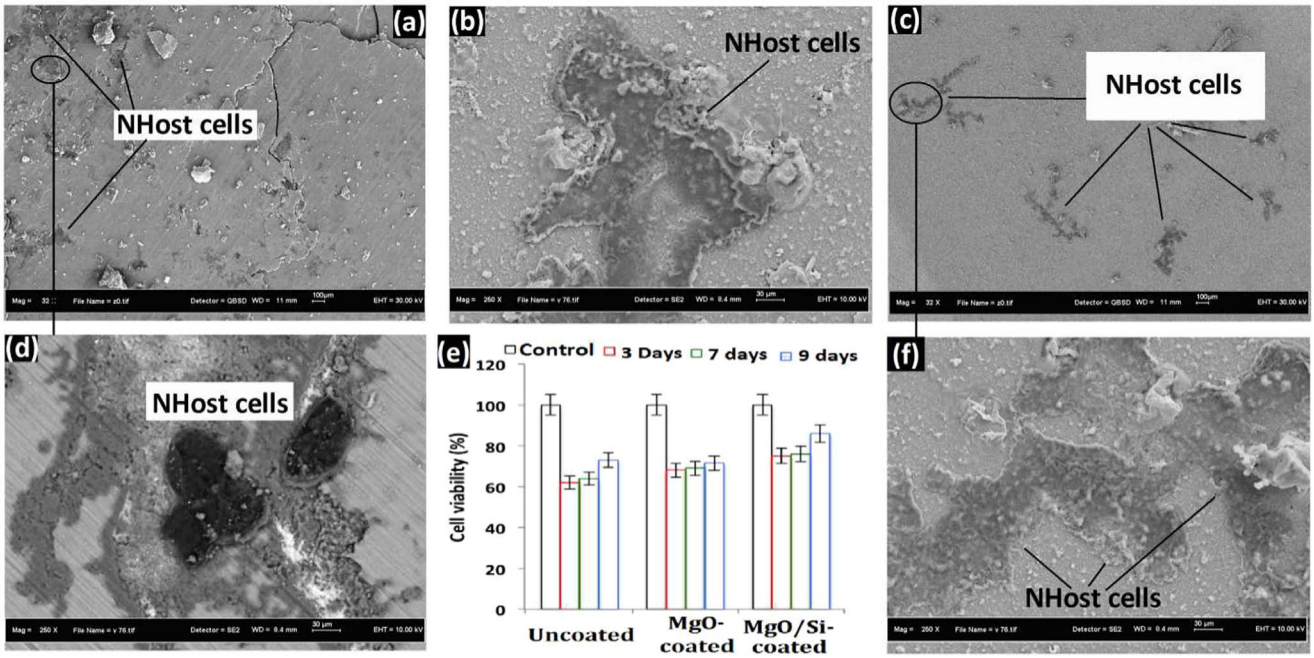

Fig. 10. FE-SEM micrographs of the cells cultured for 3 days on the surfaces of (a, d) uncoated, (b) MgO-coated, (c, f) Si/MgO-coated Mg/TiO_2/HA nanocomposites, which evidently indicate the adhered cells on the surfaces (arrows) and (e) MTT assay results indicate normal human osteoblast (NHOst) cells proliferating on the uncoated, MgO-coated and Si/MgO-coated Mg/TiO_2/HA nanocomposites after 3, 7 and 9 days of culture. The data are presented as mean ± SD and values with $P < 0.05$ were considered as statistically non-significant.

environment with a closer pH to the normal physiological environment by controlling rapid corrosion rate of Mg-based nanocomposite, thus benefitting cell adhesion and growth. During degredation samples, smaller amounts of Mg and alloying elements can be released from the coated samples thus giving rise to the better cell viability and cell attachment rather uncoated sample. The cell viability percent improved by increasing of incubation time, as after 9 days, it reached to 72, 71 and 84 for uncoated, MgO-coated and Si/MgO-coated samples, respectively. This enhancement can be attributed to the decline of very fast initial degradation rate of Mg-based nanocomposite by the formation corrosion products that act as the protective coverage against corrosive medium. Therefore, excessive formation of hydrogen bubbles, released metal ions and alkaline environment that resulted by the rapid degradation of Mg-based samples are restricted by the precipitation of corrosion products on the surface of samples. Thereby, less hydrogen evolution by Si/MgO and MgO coatings are providing more stable surfaces with better biocompatibility than bare nanocomposite. Fig. 10 shows the FE-SEM morphology of the cultured cells for 72 h on the surfaces of uncoated, MgO-coated and Si/MgO-coated samples, which clearly indicates the adhered cells (shown by arrows) on the surfaces. With regards the FE-SEM micrographs and cell viability test, Si/MgO-coated nanocomposite exhibits good cell adhesion and viability. It is possibly because of the formation a anti-corrosion, hydrophobic, and biocompatible surface coating containing Si and MgO layers. Other surface characteristics, such as surface roughness, chemical composition, as well as surface energy, can also affect the cell responses (cell spreading, adhesion, and proliferation). The surface energy of the implantable materials as another important effective factor on the cellular behavior can regulate cell adhesion, spreading, and proliferation. Hence, better cell attachment can be resulted by the lower surface energy on the coated samples (Jin et al., 2015). Some researchers have studied the relationship between the surface energy, contact angle and cellular behavior. As it was reported, the surface interactions are very complex issues and surface free energy is not only correlated to wettability that can be measured using contact angle test. However, the water contact angle measurement is one of the approaches to evaluate surface tension. Furthermore, with regards one general observation, the hydrophobic surfaces with larger water contact angles are beneficial to cell adhesion and proliferation (Kennedy et al., 2006; Padial-Molina et al., 2011). In some studies, a 60–70° contact angle is reports as the ideal range for cell attachment and spreading, as well as 65° water contact angle is commonly regarded as the magical value for implantable materials (Gentleman and Gentleman 2014; Groth and Altankov, 1996). The surface tension energy decreased from 63.14 in uncoated sample to 56.68 and 47.55 dyne/cm for MgO-coated and Si/MgO-coated nanocomposites; however, the contact angle increased from 32° to 47° and 62° (Fig. 3), respectively, thus boding well for osteoblasts. As be observed in Fig. 10a and d, the NHost cells cultured on the uncoated sample spread less and also have a more abnormal shape compared to cells, which adhered and spread well on the MgO-coated nanocomposite with a normal shape (Fig. 10b). The NHost cells cultured on the surface Si/MgO coated sample are large in number and spread very well by 3 days of incubation (Fig. 10c and f). There is a higher tendency to better proliferation among the cells that spread better; as, good cell attachment is an important parameter for promoting proliferation (Gu et al., 2016).

3.4. Mechanical properties

With regards to our investigations, the Mg/TiO_2/HA nanocomposite covered by MgO and Si/MgO coatings clearly indicate appropriate properties for orthopedic applications. During the service period, sufficient strength is required for implant materials that are used in load-bearing applications as the damaged tissue has sufficient time to heal. Thus, after and before immersion of the bare and coated samples in SBF, the influence of coatings on the mechanical properties of samples was evaluated using compression test. As known, the surfaces of metal-based materials fabricated using powder metallurgy route often covered by the oxide layer, which affect the mechanical properties of these materials. The disruption of contact between the close magnesium particles is occurred by the oxidation of raw powder particles (Muhammad et al., 2011) that restricts the adhesion of powder particles of magnesium to each other's (Esen, 2011). It can cause pre-mature fracture and poor bonding among the particles under compression loading (Krishnamurthy et al., 1991). Therefore, the uncoated samples machined before mechanical compression tests to remove oxide layers. As shown in Fig. 11c and c1, at the cold pressing stage of PM process, poor densification the regions close to the edges and less adhesion of powder particles to each others in this region of pellets that caused by the high friction between powder particles and the compaction die led to appearance the premature inter-particle cracks and delamination at the edge of samples, as the sharp edges can not be observed in the uncoated pellets (Dezfuli et al., 2017). As be seen in Fig. 11a and b, the edge of uncoated sample rupture from the core part of the sample after compressive mechanical tests; moreover, the shells and delamination with poor adhesion to the core that are dominant at the edges of the uncoated sample were produced and vertically propagated by compression and finally resulted in failure the sample. However, the core part of samples plastically deformed that can be caused by the occurrence twinning during compressive tests (Fig. 11a). At grain boundaries of polycrystalline material, the strain incompatibility produced with the constraints that applied by close grains introduced the extra stresses to obtain strain compatibility at these regions. The twins and non-basal dislocations (e.g. $< c+a >$) may be activated by these compatibility stresses, at room temperature. When the amount of stress incompatibility is relatively low, twinning has the privilege to initiate since the critical resolved shear stress (CRSS) for the $< c+a >$ slip (40 MPa) (Obara et al., 1973) is much higher than that for twining (2–3 MPa) (Reed-Hill and Robertson, 1957). The surface characteristics have effective influence on the mechanical properties of metal matrix composites. As be seen in Fig. 11e and g, the delamination and inter-particle crack tendency at the edge of samples almost disappeared by coatings that can improve the ductility samples during compression loading. Fig. 12a shows the stress-strain curves of uncoated and coated samples after PM process and before immersion in SBF. The compression test also performed on the pellets of pure Mg (fabricated using pure powders of magnesium) to compare of mechanical behavior with uncoated and coated nanocomposites. A high compressive failure strain (8.1%) was not obtained for the uncoated sample due to the surface delamination and early inter-particle fracture in edges, which led to the premature failure. The ultimate compressive strength (UCS) of MgO-coated sample (151 MPa) is close to that of the uncoated one (160 MPa); however, the enhancement in compressive failure strain to the higher percentage can be attributed to the better formability MgO coating as one of the main components of bio-glasses (Anand et al., 2016) that can delay growth of the surface cracks and failure of sample. Moreover, assembling of MgO layer on the surface of nanocomposite cover the inter-particle cracks, which existed specially in the edge of uncoated samples. As can be seen in Fig. 11g, the edge of MgO-coated sample is sharp, almost free of delamination and inter-particle cracks that can propagate and fail the sample during compression tests. By fabrication of Si layer as the second layer of coating on top of the MgO layer (as inner layer of coating), UCS and the compressive failure strain both decreased compared to those of the MgO-coated sample (Table 2), which can be caused by the presence of micro-cracks on the surface of Si-coated sample. Moreover, the hard and irregular-shaped Si particles with multiple edges could act as an indenter and create some cracks on the surface of samples, which disrupt the magnesium-oxide layer and can propagate inside the substrate of nanocomposites; as a result these cracks fail the sample by continuing compression. Fig. 10h shows some cracks along the interface of MgO and Si coatings, which are being arisen during compression test. Additionally, the low plasticity and

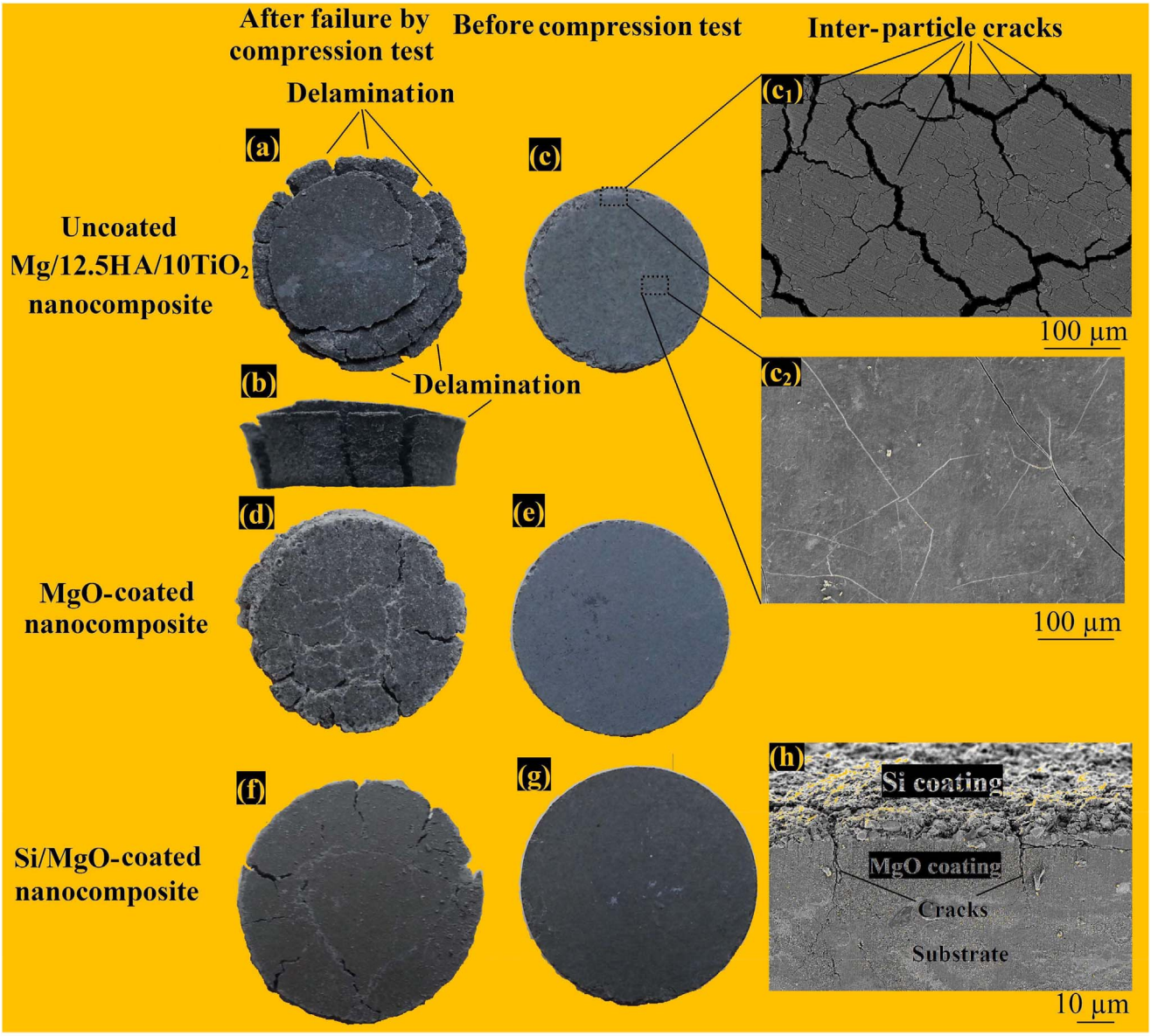

Fig. 11. Surface Photographic images of (c) uncoated, (e) MgO-coated, (g) Si/MgO-coated Mg/TiO_2/HA pellets before compression test, (a) uncoated, (b) cross-sectional photograph uncoated, (d) MgO-coated and (f) Si/MgO-coated Mg/TiO_2/HA pellets after mechanical compression test. Surface FE-SEM images of (c1, c2) uncoated Mg/TiO_2/HA nanocomposites before mechanical compression test and cross-sectional FE-SEM image (h) Si/MgO-coated Mg/TiO_2/HA nanocomposite after compression.

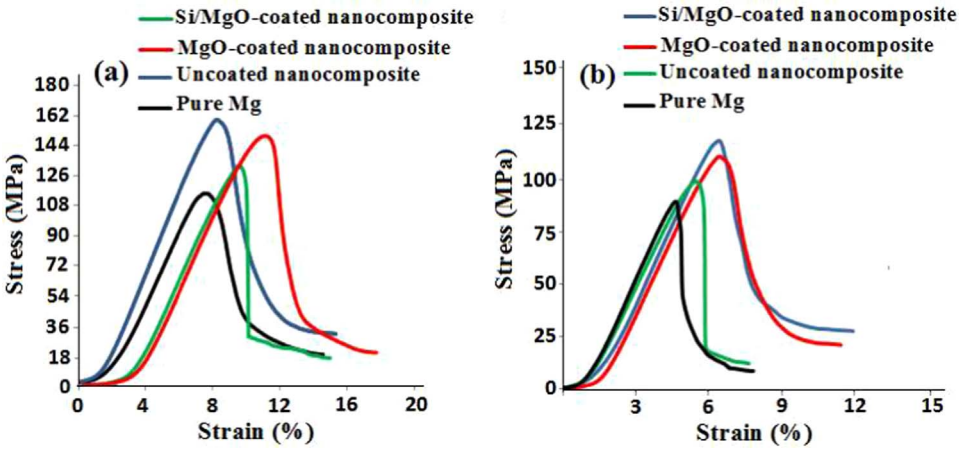

Fig. 12. Compressive stress–strain curves of the uncoated, MgO-coated and Si/MgO-coated Mg/TiO_2/HA nanocomposites (a) before and (b) after 28 days of immersion in SBF solution at 37 °C.

Table 2
Ultimate compressive strength and compressive failure strain of the uncoated and coated Mg/15TiO_2/5HA nanocomposites before and after 28 days of immersion in SBF at 37 °C.

Sample	Before immersion		After 28 days of immersion in SBF at 37 °C	
	Ultimate compression strength–UCS (MPa)	Compressive failure strain (%)	Ultimate compression strength–UCS (MPa)	Compressive failure strain (%)
Pure Mg	115	7.3	87	4.5
uncoated	160	8.1	98	5.2
MgO/coated	151	11.2	107	6.3
Si/MgO-coated	133	9.6	118	6.2

formability of Si particles led to low densification and compactness of these particles in outer layer. Thus, there are some pores and micro-cracks between Si particles that can act as a place for stress concentration and failure the sample. After partial degradation of samples, the residual strength of bio-devices should be measured as an important factor to evaluate mechanical performance of samples. Therefore, the compression tests performed on the immersed samples for 4 weeks in the SBF solution. By 28 days of immersion in SBF, the uncoated sample lost 38% of its mechanical strength owing to the fast degradation rate (Fig. 12b). However, the gradual losses were observed in mechanical properties of coated samples by slower corrosion rates. The mechanical integrity of samples is being deteriorated by progress of degradation due to the interaction stress and corrosion on each other's. The presence of premature cracks on the edges of uncoated sample intensified the degradation of samples as be observed in Fig. 9e, f and l. on the other hand, the degraded area on the surfaces of immersed uncoated sample accelerated the progress of deterioration of integrity during mechanical loading. The corrosion pits appeared on the degraded samples subjected to immersion tests in SBF solution are the suitable sites for nucleation of the mechanical cracks. Thus, the mechanical strength of samples gradually loses by pitting corrosion as the main responsible factor. Furthermore, the mechanical cracks intensify the growth and initiation of more amounts of the corrosion pits as it observed in Fig. 9p and r more corrosion pits with bright color appeared close to the cracks. In addition, during socking samples in SBF, the dissolution of some parts of magnesium as the main component of composites proofed by the density measurements, it led to the formation porosities inside the matrix of composites that deteriorate the mechanical properties of immersed samples. The ultimate compressive strength and compressive failure strain the uncoated and coated Mg/15TiO_2/5HA nanocomposite before and after 28 days of immersion in SBF are compared and listed in Table 2. After immersion, The Si/MgO-coated sample indicates the best mechanical properties with 6.3% compressive failure strain and ultimate compression strength at 118 MPa that is still close to the strength range of cortical bone (130–180 MPa (Axen et al., 2003; Bureau et al., 2006)).

4. Conclusion

In summary, MgO-coated and Si/MgO-coated Mg/15TiO_2/5HA bionanocomposite fabricated using PM technique. The XRD, XPS, EDS and FE-SEM results confirmed that mono layer MgO and double layer Si/MgO as the protective coatings bonded onto the surface of Mg/TiO_2/HA bionanocomposite to control the degradation rate in physiological environment. Electrochemical Impedance Spectroscopy, Potentiodynamic polarization and immersion test support that the anticorrosion ability of Mg/TiO_2/HA has been improved significantly after surface modification. The coated samples exhibit the higher impedance and smaller corrosion current densities in SBF. Less hydrogen evolution, smaller pH variation, and much less severe corrosion are observed from the Si/MgO-coated Mg/TiO_2/HA bionanocomposite. The significant enhancement in the corrosion resistance is mainly attributed to the stable and protective Si outer layer, as well as partially protective MgO inner layer. According to the biological investigations, cells attach and spread well on the Si/MgO coating and cells incubated with the extracted medium of the Si/MgO-coated show the highest viability compared to those of the uncoated and MgO-coated samples, indicating that the Si/MgO-coated bionanocomposite has good biocompatibility in vitro. The improvement in the in vitro biological response cells resulted from the improved corrosion resistance and relatively hydrophobic surface. The presence of MgO and Si/MgO coatings on the surface of Mg/TiO_2/HA bionanocomposite improved the compressive failure strain of samples, before and after degradation in SBF. After 28 days of immersion in SBF, the reduced degradation rates of the MgO- and Si/MgO-coated bionanocomposites led to the slower losses of the strength in the close values to the strength range of cortical bone. Our results suggest that Si/MgO coatings are promising method to improve the corrosion resistance, mechanical properties and in vitro biocompatibility of the Mg/TiO_2/HA bionanocomposite.

Acknowledgements

The authors would like to acknowledge the Universiti Teknologi Malaysia (UTM) and financial support under FRGS Grant Numbers 4F608, 09H80, 4F648 and 4F808.

References

Amiri, H., Mohammadi, I., Afshar, A., 2017. Surf. Coat. Technol. 311, 182–190.
Anand, I., Singh, K., J., Kaur, K., Kaur, H., Arora, D., S., 2016. Ceram. Int. 42, 3638–3651.
Atrens, A., Liu, M., Abidin, N., I., Z., 2011. Mater. Sci. Eng. B. 176 (20), 1609–1636.
Axen, N., Hermansson, L., Persson, T., Bjoerklund, K., Kraft, L., 2003. Ceramic Material and Process for Manufacturing. Google Patents.
Brink, M., 1997. J. Biomed. Mater. Res. 36 (1), 109–117.
Bureau, M.N., Legoux, J.G., Denault, J., 2006. Implantable Biomimetic Prosthetic Bone. Google Patents.
Chang, J., K., Chen, S., Y., Tsai, W., T., Deng, M., J., Sun, I., W., 2007. Electrochem. Commun. 9 (7), 1602–1606.
Chen, Y., Yan, G., Wang, X., Qian, H., Yi, J., Huang, L., 2015. Surf. Coat. Technol. 269, 191–199.
Chen, Z., Huang, L., Zhang, G., Qiu, Y., Guo, X., 2012. Corros. Sci. 65, 214–222.
Choi, H., Y., Kim, W., J., 2016. J. Alloy Compd. 664, 25–37.
Del Campo, R., Savoini, B., Muñoz, A., Monge, M.A., Pareja, R., 2017. J. Mech. Behav. Biomed. Mater. 69, 135–143.
Dezfuli, S., N., Leeflang, S., Huan, Z., Chang, J., Zhou, J., 2017. J. Mech. Behav. Biomed. Mater. 67, 74–86.
Ebisawa, Y., Kokubo, T., Ohura, K., Yamamuro, T., 1990. J. Mater. Sci.-Mater. M 1 (4), 239–244.
Esen, Z., 2011. Magnesium Technology. Wiley, San diego.
Fintova, S., Kunz, L., 2015. J. Mech. Behav. Biomed. Mater. 42, 219–228.
Groth, T., Altankov, G., 1996. Biomaterials 17 (12), 1227–1234.
Guan, R., G., Johnson, I., Cui, T., Zhao, T., Zhao, Z., Y., et al., 2012. Biomed. Mater. Res. A 100, 999–1015.
Gu, C., D., Yan, W., Zhang, J., L., Tu, J., P., 2016. Corros. Sci. 106, 108–116.
Gu, K., Lv, L., Lu, Z., Yang, H., Mao, F., Tang, J., 2013. Corros. Sci. 74, 408–413.
Gu, X.N., Li, N., Zhou, W., R., Zheng, Y., F., Zhao, X., Cai, Q., Z., 2011. Acta Biomater. 7 (4), 1880–1889.
Gu, Xuenan, Zhou, W., Zheng, Y., Dong, L., Xi, Y., Chai, D., 2010. Mater. Sci. Eng. C 30 (6), 827–832.
Heublein, B., Rohde, R., Kaese, V., Niemeyer, M., 2003. Heart 89 (6), 651–656.
Hornberger, H., Virtanen, S., Boccaccini, A.R., 2012. Acta Biomater. 8 (7), 2442–2455.
Ibrahim, H., Klarner, A., D., Poorganji, B., Dean, D., Luo, A., A., Elahinia, M., 2017. J. Mech. Behav. Biomed. Mater. 69, 203–212.
Jin, W., Wu, G., Feng, H., Wang, W., Zhang, X., Chu, P., K., 2015. Corros. Sci. 94, 142–155.
Kasuga, T., Nakagawa, K., Yoshida, M., 1987. J. Mater. Sci. 22 (10), 3721–3724.
Kennedy, Scott B., Washburn, N.R., Simon, C.G., Amis, E.J., 2006. Biomaterials 27 (20),

3817–3824.
Khalajabadi, Shahrouz Zamani, Abdul Kadir, M.R., Izman, S., Samavati, A., Othaman, Z., 2015. Ceram. Int. 41 (9, Part A), 11346–11358.
Khalajabadi, Shahrouz Zamani, Ahmad, N., Izman, S., Abu, A.B.H., Haider, W., Kadir, M.R.A., 2017. J. Alloy Compd. 696, 768–781.
Khalajabadi, Shahrouz Zamani, Ahmad, N., Yahya, A., Yajid, M., Samavati, A., et al., 2016. Ceram. Int. 42 (16), 18223–18237.
Khan, Ather Farooq, Saleem, M., Afzal, A., Ali, A., Khan, A., Khan, A.R., 2014. Mater. Sci. Eng. C 35, 245–252.
Kokubo, T., 1991. Biomaterials 12 (2), 155–163.
Kokubo, Tadashi, Takadama, Hiroaki, 2006. Biomaterials 27 (15), 2907–2915.
Krishna, L., R., Poshal, G., Jyothirmayi, A., Sundararajan, G., 2015. Mater. Des. 77, 6–14.
Krishnamurthy, S., Weiss, I., Froes, F., 1991, 29, pp. 135–146.
Li, J., Song, Y., Zhang, S., Zhao, C., Zhang, F., Zhang, X., 2010. Biomaterials 31 (22), 5782–5788.
Li, M., Cheng, Y., Zheng, Y., Zhang, X., Xi, T., Wei, S., 2013. J. Mater. Sci. Technol. 228, S262–S265.
Li, Zhijun, Yuan, Yi, Jing, Xiaoyan, 2017. J. Alloy Compd. 706, 419–429.
Lin, D., J., Hung, F., Y., Jakfar, S., Yeh, M., L., 2016. Mater. Des. 89, 235–244.
Lin, X., Tan, L., Wan, P., Yu, X., Yang, K., Hu, Z., Li, Y., 2013. J. Mater. Sci. Technol. 232, 899–905.
Liu, P., Pan, X., Yang, W., Cai, K., Chen, Y., 2012. Mater. Lett. 75, 118–121.
Lu, Y., Tan, L., Xiang, H., Zhang, B., Yang, K., Li, Y., 2012. J. Mater. Sci. Technol. 28 (7), 636–641.
Meischel, M., Eichler, J., Martinelli, E., Karr, U., a., Weigel, J., et al., 2016. J. Mech. Behav. Biomed. Mater. 53, 104–118.
Mohedano, M., Blawert, C., Zheludkevich, M.L., 2015. Mater. Des. 86, 735–744.
Mostaed, E., Sikora-Jasinska, M., Mostaed, A., Loffredo, S., Demir, A.G., et al., 2016. J. Mech. Behav. Biomed. Mater. 60, 581–602.
Muhammad, W.N.A.W., Sajuri, Z., Mutoh, Y., Miyashita, Y., 2011. J. Alloy. Compd. 509, 6021–6029.
Nayak, S., Bhushan, B., Jayaganthan, R., Gopinath, P., Agarwal, R., D., Lahiri, D., 2016. J. Mech. Behav. Biomed. Mater. 59 (57–70).
Obara, T., Yoshinga, H., Morozumi, S., 1973. Acta Metall. 21, 845–8853.
Oliveira, J.M., Correia, R.N., Fernandes, M.H., 2000. J. Non-Cryst. Solids 265 (3), 221–229.
Padial-Molina, Miguel, Galindo-Moreno, P., Fernández-Barbero, J., E., O'Valle, F., Jódar-Reyes, A., B., et al., 2011. Acta Biomater. 7 (2), 771–778.
Paital, S.R., Dahotre, N.B., 2009. Mat. Sci. Eng. R 66 (1–3), 1–70.
Pan, Chang-Jiang, Hou, Y., Wang, Y., N., Gao, F., Liu, T., et al., 2016. Mater. Sci. Eng. C 67, 132–143.
Qi, Guochao, Zhang, S., Khor, K., A., Weng, W., Zeng, X., Liu, C., 2008. Thin Solid Films 516 (16), 5172–5175.
Qi, Pengkai, Qi, P., Yang, Y., Zhao, S., Wang, J., Li, X., et al., 2016. Mater. Des. 96, 341–349.
Reed-Hill, R.E., Robertson, W.D., 1957. Acta Metall. 5, 717–727.
Rosalbino, F., De Negri, S., Saccone, A., Angelini, E., 2010. J. Mater. Sci.-Mater. M 21 (4), 1091–1098.
Ryu, H., Sheng, N., Ohtsuka, T., Fujita, S., Kajiyama, H., 2012. Corros. Sci. 56, 67–77.
Shadanbaz, S., Dias, G.J., 2012. Acta Biomater. 8 (1), 20–30.
Shi, L.-L., Huang, Y., Yang, L., Feyerabend, F., Mendis, C., et al., 2015a. J. Mech. Behav. Biomed. Mater. 47, 38–48.
Shi, Ping, Niu, B., Chen, S.E., Y., Li, Q., 2015b. Surf. Coat. Technol. 262, 26–32.
Shi, Zhiming, Liu, Ming, Atrens, Andrej, 2010. Corros. Sci. 52 (2), 579–588.
Song, G., 2007. Corros. Sci. 49 (4), 1696–1701.
Taleatu, B.A., Omotoso, E., Lal, C., Makinde, W.O., Ogundele, K.T., et al., 2014. Surf. Interface Anal. 46 (6), 372–377.
Wang, Congjie, Zhu, S., Wang, L., Feng, Y., Ma, X., Guan, S., 2015a. J. Alloy. Compd. 621, 53–61.
Wang, M.-J., Li, C.-F., Yen, S.-K., 2013. Corros. Sci. 76, 142–153.
Wang, Q., Tan, L., Yang, K., 2015b. J. Mater. Sci. Technol. 31 (8), 845–851.
Watts, S.J., Hill, R.G., O'Donnell, M.D., Law, R.V., 2010. J. Non-Cryst. Solids 356 (9–10), 517–524.
Wolf, F.I., Cittadini, A., 2003. Mol. Asp. Med. 24 (1–3), 3–9.
Wu, Chengtie, Chang, Jiang, 2007. J. Biomed. Mater. Res.-A 83 (1), 153–160.
Yang, Huawei, Xia, K., Wang, T., Niu, J., Song, Y., et al., 2016. J. Alloy. Compd. 672, 366–373.
Zartner, P., Buettner, M., Singer, H., 2007. Catheter. Cardiovasc. Interv. 69 (3), 443–446.
Zhang, C.Z., Zhu, S., J., Wang, L., G., Guo, R., M., Yue, G., C., 2016a. Mater. Des. 96, 54–62.
Zhang, D., Wei, B., Wu, Z., Qi, Z., Wang, Z., 2016b. Surf. Coat. Technol. 303, 94–102.
Zhang, S., Zhang, X., Zhao, C., Li, J., Song, Y., et al., 2010. Acta Biomater. 6 (2), 626–640.
Zhao, L., Cui, C., Wang, Q., Bu, S., 2010. Corros. Sci. 52 (7), 2228–2234.
Zhao, Ming-Chun, Liu, M., Song, G.-L., Atrens, A., 2008. Corros. Sci. 50 (11), 3168–3178.
Zhao, M., C., Schmutz, P., Brunner, S., Liu, M., Song, G., 2009. Corros. Sci. 51 (6), 1277–1292.
Zheng, Y.F., Gu, X.N., Witte, F., 2014. Mater. Sci. Eng. R 77, 1–34.
Zomorodian, A., Garcia, M., P., e Silva, T., M., Fernandes, J., C., S., 2013. Acta Biomater. 9 (10), 8660–8670.